Acta Materialia 279 (2024) 120206

Contents lists available at ScienceDirect

Acta Materialia

journal homepage: www.elsevier.com/locate/actamat

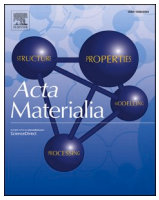

Full length article

Elucidating the role of Cr migration in Ni-Cr exposed to molten FLiNaK via multiscale characterization

Sean H. Mills [a,b,*], Ryan D. Hayes [c], Nathan Bieberdorf [a,e], Steven E. Zeltmann [a], Alexandra M. Kennedy [c], Laurent Capolungo [d], Mark Asta [a,e], Raluca O. Scarlat [c,**], Andrew M. Minor [a,b,*]

[a] Department of Materials Science and Engineering, University of California, Berkeley, CA, USA
[b] National Center for Electron Microscopy, Molecular Foundry, Lawrence Berkeley National Laboratory, Berkeley, CA, USA
[c] Department of Nuclear Engineering, University of California, Berkeley, CA, USA
[d] Materials Science and Technology, Los Alamos National Laboratory, Los Alamos, NM 87545, USA
[e] Materials Sciences Division, Lawrence Berkeley National Laboratory, Berkeley, CA, USA

ARTICLE INFO

Keywords:
Corrosion
STEM HAADF
Scanning electron microscopy (SEM)
Phase field modeling
Four-dimensional scanning electron microscopy (4DSTEM)
Energy dispersive spectroscopy (EDS)
Inductively coupled plasma optical emission spectroscopy (ICP-OES)

ABSTRACT

Structural materials used in nuclear reactor environments are subjected to coupled extremes such as high temperature, irradiation, and corrosion which act in concert to degrade their functional performance. Connecting alloy microstructure such as grain boundaries, and accumulating point defects with corrosion attack and pore morphology is critical to understanding underlying mechanisms. We uncover the compositional variations and morphology at multiple length scales in corrosion-damaged Ni-Cr alloy after exposure to oxidants in molten fluoride salts. A complex network of dense corrosion pores is detected by surface-level SEM observations. The corrosion pores take on a 1-dimensional morphology and are enriched with Ni and depleted of Cr 1–5 μm from the pore surface. STEM-EDS and 4D-STEM strain maps acquired simultaneously highlight the local variations in composition and structure of $a \leq 200$ nm Cr-rich layer identified from a cross-section taken at the bottom of an isolated corrosion pore between the Ni-Cr alloy matrix and the embedded salt. However, the absence of an observed interface between the Ni-Cr alloy matrix and the FCC-structured Cr-rich layer suggests that Cr plating from the salt did not transpire. These findings support a proposed Cr lattice diffusion mechanism rather than Cr-precipitation from the salt to accommodate temperature transient conditions during sample cooling. Through the development of a 1D phase field model, these results are rationalized by formation energies for the Ni- and Cr-oxidation into the molten salt. This study reveals the locally altered microstructure caused by high temperature corrosion in non-steady-state molten salt nuclear reactor environments.

1. Introduction

Corrosion in metals [1] is a leading factor underlying failure of essential components in aerospace [2], infrastructure [3] and nuclear energy production [4]. Extensive research is performed to predict failure of metallic components from mechanisms such as stress corrosion cracking (SCC) [5,6], irradiation-assisted stress corrosion cracking (IASCC) [7] and environmentally assisted cracking (EAC) [8]. Specifically, nuclear reactor components are constantly subjected to a variety of challenging environments such as high temperatures and non-steady state temperature gradients, irradiation exposure, and corrosion through direct contact with the reactor coolant. Material degradation in these systems originates at the microscale and nanoscale where, for example, corrosion attack is governed by the chemistry of the liquid in contact with the metal (aqueous, molten salts, etc.), thermal history, and existing microstructural features such as grain boundaries and accumulating point defects [9]. Therefore, multimodal and multiscale approaches are needed to characterize these difficult-to-detect points of failure to connect the underlying mechanisms to macroscopic properties to design materials for longer lifespans in next-generation nuclear reactor systems [10].

Molten salt reactors (MSRs) are next-generation nuclear reactors that

* Corresponding authors at: Department of Materials Science and Engineering, University of California Berkeley, Berkeley, CA 94720, USA.
** Corresponding author at: Department of Nuclear Engineering, University of California Berkeley, Berkeley, CA, 94720, USA.
E-mail addresses: seanmills@berkeley.edu (S.H. Mills), scarlat@berkeley.edu (R.O. Scarlat), aminor@berkeley.edu (A.M. Minor).

https://doi.org/10.1016/j.actamat.2024.120206
Received 1 December 2023; Received in revised form 12 July 2024; Accepted 17 July 2024
Available online 18 July 2024

employ molten salts [11] as a more effective coolant than pressurized water, for example, and can use molten salt as fuel components in some cases. Molten halides have a low vapor pressure (hence a large margin to boiling even at ambient pressure and above 1000 °C temperatures) and desirable thermo-physical properties that can be applied towards inherent safety features and passive safety systems in nuclear reactors [10–18]. Ongoing research is underway to study the degradation of salt facing components. Controlled corrosion of structural materials exposed to molten salts, particularly at high temperatures (general operating temperatures up to 600–750 °C [10,15]), is of relevance to development of MSRs and fluoride salt-cooled high-temperature reactors (FHRs).

For a metal alloy facing a molten salt of a given redox potential, different constituent alloying elements will oxidize and dissolve in the salt differently, as determined by the Gibbs free energy of formation of the metal halide of that element [4,15,19,20]. At high temperature, the formation of a passive oxide layer would be suitable for protecting the material, however, the oxygen content within the salt is minimized to avoid precipitation of fissile material within the reactor [9,15]. As such, oxide layers formed in molten salt environments are neither stable nor protective.

For Ni-Cr alloys, direct corrosion by the molten salt tends to proceed via selective oxidation and dissolution of the less-noble Cr from the alloy [12,16]. Importantly, the associated corrosion rate and morphology [17, 21,22] will also depend on transport of the corrosion reactants (e.g. Cr in the metal and oxidizers in the molten salt, such as EuF_3) to the interface, the transport of corrosion products (e.g. oxidized Cr in the molten salt) away from the interface, and the transport of the residual more-noble Ni at the dealloyed interface [17]. These simultaneous processes are illustrated in Fig. 1a. For the Ni-Cr in molten-chloride salts, these processes have been shown to synergistically lead to rapid dealloying corrosion towards formation of bicontinuous Ni-rich structures [17,18,22,23]. However, for Ni-Cr in molten-fluoride salts, such as LiF-NaF-KF eutectic (FLiNaK), which is the focus of the present work, these dealloying processes can be confined to singular corrosion channels or 1-D "wormholes" [21], schematically illustrated in Fig. 1b. Similar discrete corrosion channels have also been seen in more complex engineering alloys, and are often initiated at grain boundaries [24–26].

While the aforementioned studies revealed key details regarding the roles of Cr transport and dissolution, and also Ni transport, several outstanding questions remain regarding how these processes couple with local changes in structure and composition at the metal-salt interface. Advancing such understanding requires detailed knowledge of the nanoscale interfacial composition and structure, which influence atomistic processes underlying the corrosion rate and associated morphologies. To date, there is no such detailed nanoscale experimental characterization of these interfaces.

An objective of the present work is to advance and apply state-of-the-art electron microscopy methods to provide detailed characterization of metal-salt interfaces at the nanoscale. We focus on regions at the corrosion front, deep inside the tortuous corrosion channels that penetrate into the alloy. These narrow and tortuous corrosion pores have been hypothesized to limit transport of the corrosion products and reactants [18,27]. A complete mechanistic description of how these factors synergistically control the corrosion rate and morphology is lacking. Thus, a clear visualization of the metal-salt interface is required where diffusion, redox reactions, and dissolution processes are expected to be simultaneously active.

In this study, we investigate how the intricate mechanisms underlying molten salt corrosion control the microstructure near the metal-salt interface. Specifically, we examine corrosion of $Ni_{80}Cr_{20}$ metal alloy exposed to molten LiF-NaF-KF eutectic salt (FLiNaK) at 600 °C with 5 wt.% EuF_3 added and use a high spatial and temporal resolution S/TEM-based approach to characterize the microstructure of resultant 1-D corrosion channels that infiltrate deep inside the metal. We have chosen here to examine one of the deepest corrosion pores to characterize a location where the corrosion reaction is presumed to have been most active. Depending on its concentration in the salt, EuF_3 sets a corrosion potential in the salt that is (1) relevant to reactor conditions and (2) suppresses other environmentally driven processes, such as ingress of oxygen and moisture in the glovebox or ppm scale impurities within the salt [15,28,29]. By focusing on the metal-salt interface, we consider how the interplay between the local dissolution of Cr and redistribution of Ni affects the corrosion process. For post-corrosion characterization, we utilize techniques such as inductively coupled plasma optical emission spectroscopy (ICP-OES) and energy dispersive spectroscopy (SEM-EDS) to detect changes in composition and morphology at the microscale, associated with non-uniform corrosion damage that take the form of salt-filled pores. We propose an alternative scenario that reflects molten salt corrosion by highlighting active Cr transport and dissolution, combined with Ni redistribution. To confirm this, we investigate a rapid mass-flow pathway concentrated at the bottom of a salt-filled corrosion pore (Fig. 1b), where the corrosion reaction is most active. We connect nano-scale changes in composition and structure within a salt-filled pore through simultaneous STEM-EDS and 4D-STEM mapping. Further, we employ a 1D phase field model to rationalize experimental observations and assess the role of corrosion driving forces on nanoscale chemical redistribution at the metal-salt interface.

2. Methods

2.1. Materials and processing

Ni (80 at.%) Cr (20 at.%) metal alloy rods (3 mm diameter, 10 mm length) of 99.999 % purity were sourced from Goodfellow Corporation (part number NI05-RD-000,110). The rods were sectioned via conventional machining methods to 2 mm tall pucks. The flat surfaces of the pucks were ultimately polished with 1200 grit silicon carbide sandpaper

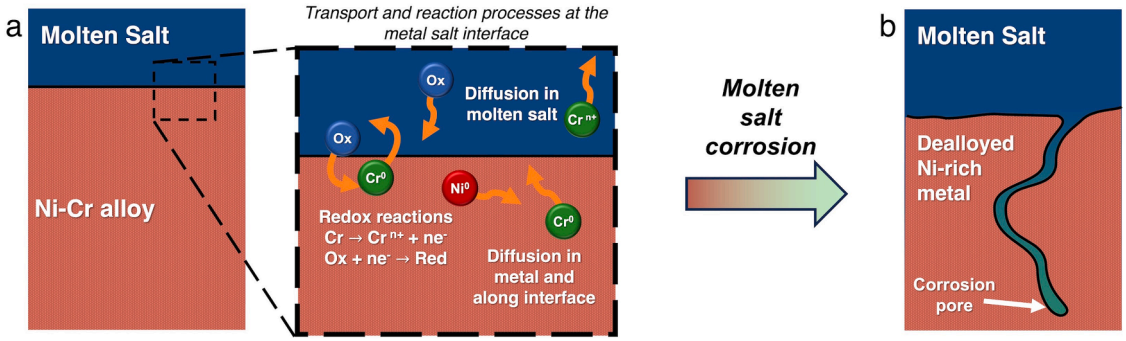

Fig. 1. Schematic illustrations describing the corrosion of a NiCr-based alloy exposed to molten salt at reactor operating temperatures. (a) Metal-salt interface before corrosion reaction. Expected reactions and transport of species at the metal-salt interface (inset of (a)). (b) 1-dimensional corrosion pore after molten salt corrosion reaction.

and sonicated in isopropanol before they were exposed to molten salt. 20 mm outer diameter round bars of the same material were fabricated into crucibles (14 mm inner diameter, 20 mm height) with matching lids via computerized numerical control milling. The sample and crucible dimensions are specified in Table 1.

2.2. Molten salt corrosion experiment

This corrosion experiment was carried out in a 700 W cylindrical furnace with an inner diameter of 76.2 mm, contained within an argon glovebox (H_2O < 1 ppm, O_2 < 3 ppm). Coarse FLiNaK and EuF_3 (Alfa Aesar, 99.98 % purity by REO) crystals were crushed into powder via mortar and pestle, weighed, and placed into the Ni-Cr crucible before heating. The FLiNaK was sourced from Oak Ridge National Laboratory as legacy salt, purified through hydrofluorination. Referred to as "Salt #1," Sulejmanovic et al. [30] provides measurements of H, O, and trace metals. The salt-filled crucible was placed at the center of the furnace and gradually heated to 600±10 °C where it was held constant. The Ni-Cr sample was placed adjacent to the crucible and exposed to the same initial heating steps as the salt bath. Once the corrosion temperature was reached, the Ni-Cr sample was submerged in the salt bath for 4.5 h, after which the crucible was allowed to cool.

Fig. 2a illustrates the molten salt corrosion experiment and quantitative measurements taken during the experimental setup and corrosion reaction are presented in Table 1. To remove the sample, the salt was remelted, and the sample was pulled from the salt using non-reactive gold-plated tweezers. At this time, salt was poured from the crucible into a glassy carbon dish and cooled. After the sample was extracted from the salt bath and cooled to room temperature, it was transported in air to the scanning electron microscope for further inspection and FIB lift-out. The post-corrosion salt was ground using an agate mortar and pestle, and approximately 100 mg was collected for elemental analysis of the salt.

2.3. Scanning electron microscopy and sample preparation via focused ion beam

Ni-Cr pucks were initially screened for surface corrosion damage with conventional scanning electron microscopy and energy dispersive spectroscopy (SEM-EDS) compositional measurements using a Thermofisher Scientific Scios 2 DualBeam FIB/SEM equipped with EDS detector (Oxford Inc.). After surface measurements were conducted, a Fischione cross-sectional polisher was used followed by FIB milling to expose the sample cross-section. The cross-section was inspected for depth of pores and composition via secondary electron imaging using an Everhart Thornley detector (ETD-SEM) at 5 kV and 0.1 nA. EDS maps were processed and rendered using Oxford AZtec EDS software package [31] and images were measured using Fiji image analysis software [32].

Once the sample was cooled, the corrosion reaction was completed, leaving solidified salt species in-tact within the corrosion pores. The corroded bulk specimen was transported in an airtight container from the glove box to the SEM chamber to minimize exposure to atmosphere. The cross-section was exposed using FIB milling procedure to reveal the salt-filled corrosion pore microstructure as shown in Supplemental Data Fig. S1a. Supplemental Data Fig. S1b shows that the crucible cross-section exhibits similar corrosion pore morphology to the sample cross-section. TEM foils were prepared by conventional FIB lift-out at site-specific locations at the bottom of corrosion pores that are visible from the bulk sample cross-section as shown in Supplemental Data Fig. S1a. Before FIB trenching and milling steps, an electron beam (lower energy) Pt layer was initially deposited to protect the bulk sample surface and then a Pt layer was deposited using the Ga^+ ion beam to minimize damage caused by incident Ga^+ ions. The lamella was lifted out using an EasyLift™ nano-manipulator, carefully positioned on the side of a post and welded to a Cu Omniprobe® lift-out grid. The thinning procedure used progressively lower beam energy beam currents to ensure the embedded salt was preserved after lift-out. The sample was thinned to < 100 nm thickness and cleaned at 5 keV and 7 pA to remove remnant Pt contamination and Ga^+ ion beam damage that occurred during sample transfer.

2.4. Simultaneous 4-dimensional scanning transmission electron microscopy and energy-dispersive electron microscopy analysis

STEM investigation was conducted at 300 kV on an image corrected Thermofisher Scientific ThemIS microscope equipped with a Bruker SuperX energy dispersive X-ray spectroscopy (EDS) detector. The Bruker windowless detector allows for high count rates with minimal dead time and fast STEM-EDS mapping. The high speed Ceta2 camera can acquire 4k × 4k images at 40 frames per second for in situ movies. Velox software was used to acquire and process STEM-EDS spectrum image data on the ThemIS TEM. The quantification process in Velox™ applies "Brown-Powell" ionization cross-section parameterization to obtain the k-factor [33,34] using all the default factors and parameters provided by the manufacturers (Thermofisher Scientific) in the Velox™ software.

4D-STEM nano-diffraction datasets were acquired via a Gatan K2-IS (2k × 2k) detector at 400 frames per second. Each dataset contains a stack of individual electron diffraction patterns taken at each scan position that are spatially dependent on a 1–3 nm probe size of the converged electron beam [35]. The field of view consists of an approximately 100 × 100 square of frames where diffraction patterns are acquired at a 0.0025 seconds per frame collection time. A custom 40 μm patterned "bullseye" circular probe forming aperture used in this 4D-STEM analysis facilitates the identification of the center of diffraction discs, thereby enhancing the accuracy of the measurement [36]. A micro-probe lens configuration was used with spot size of 8, 3.20 milli-radian convergence angle, and 0.16 $Å^{-1}$ diffraction pixel size. The signal to noise ratio was increased by machine and software binning the data to 512 × 512 pixels before computational analysis. 4D-STEM calibration data sets were acquired during each microscope session using a polycrystalline Al standard sample. These measurements were used to correct for systematic errors such as elliptical distortion, scanning drift, and STEM rotation. Processing of structure data was enabled by strain and orientation mapping scripts provided in the open source py4DSTEM software package [37]. 4D-STEM-EDS data was processed and visualized using the Hyperspy Energy-Dispersive X-ray Spectrometry (EDS) software package v1.7.1 [38].

2.5. Salt elemental analysis by microwave digestion followed by ICP-OES

In an Ar glovebox, the entire salt used for corrosion was removed from the corrosion crucible by pouring out of the crucible while the crucible is hot. The post corrosion salt sample (38salt201) was ground using an agate mortar and pestle in a glovebox for approximately two minutes for homogenization. Approximately 88.2(1) mg of powdered

Table 1
Samples conditions of Ni-Cr exposed to molten FLiNaK + EuF_3 at 600±10 °C for 4.5 h.

Metal alloy Composition (at. %)	FLiNaK (g)	EuF3 (g)	Sample surface area (mm^2)	Sample mass (g)	Salt-facing crucible surface area (mm^2)	Total salt-facing surface area (mm^2)	Upper bound for expected Cr depletion to CrF_3 (mg)	Lower bound for expected Cr depletion depth (μm)
$Ni_{80}Cr_{20}$	2.3447	0.1139	33	0.1139	493	526	< 9.4	> 11.8

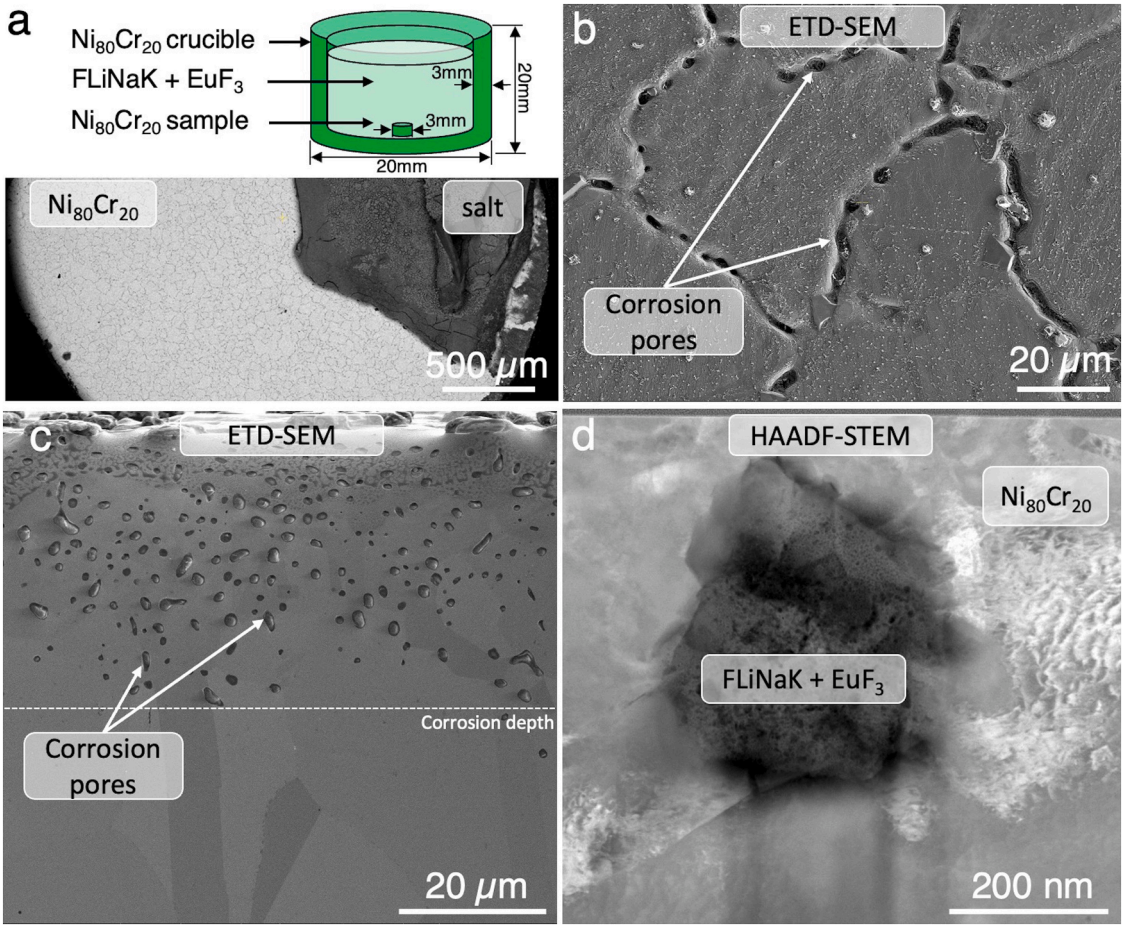

Fig. 2. Molten salt corroded $Ni_{80}Cr_{20}$ (a) schematic illustration of the molten salt corrosion experiment contained in a custom Ni-Cr crucible, and bulk Ni-Cr sample puck that is submerged in molten FLiNaK + EuF_3. (b) ETD-SEM image of the polished Ni-Cr sample surface after exposure to FLiNaK + EuF_3 salt. Dark contrast features are grain boundaries that are decorated by corrosion pores and embedded salt. (c) ETD-SEM image of a window prepared on the sample cross-section via FIB milling. The exposed pores are randomly organized, disconnected from one another, and show a consistent salt penetration through $\leq$ 40 μm of sample thickness. (d) STEM-HAADF image of a FIB lift-out specimen extracted from the bottom of a salt-filled pore located within (c) at the observed corrosion depth.

salt was measured and transferred separately to a corresponding 40 ml quartz microwave digestion tube lined with a polytetrafluoroethylene liner. Another microwave digestion tube was prepared the same way for a blank, with no salt, to account for any matrix effects. To each digestion tube, 8.0 ml HNO_3, 4.0 ml HCl, and 3.0 ml deionized H_2O is added; and measurements were made volumetrically using a graduated cylinder. Microwave digestion was performed using The CEM Focused Microwave™ Digestion System, Discover SP-D 80, and the Synergy-D Software v1.24 (2017). After digestion, samples were transferred to 50 ml Corning polypropylene centrifuge tubes (Corning™ 430,897) and topped to 50(3) ml with deionized water volumetrically using the markings on the tube, then analyzed with no further dilution.

Inductively Coupled Plasma Optical Emission Spectroscopy (ICP-OES) was performed on a Perkin Elmer 5300 DV optical emission ICP with auto sampler using WinLab32 software. A calibration curve is produced from single element standards purchased with a concentration of 100 ug/mL for Ni and Cr and 1000ug/mL for Eu from Inorganic Ventures; calibration points fall above and below the measured analyte concentrations in the digest. A 0.0 ppm standard was created using the same matrix as the standards (2 % for Ni and Cr, and 7 % for Eu (v/v) HNO_3). Each sample was analyzed in triplicate on the ICP-OES instrument. The raw data from microwave digestion and ICP-OES analysis of the digests is provided in Supplemental Data Fig. S5 and Table S1.

2.6. Phase field model for dealloying of Ni-Cr in molten FLiNaK

A phase field model was developed to compute the concentration of Ni and Cr that develop in the metal, molten salt, and across their interface during the dealloying process. The phase field model was based on the thermodynamic description used in [39] for a ternary, two-phase system, using the multi-phase field formalism proposed in [40]. The local volume fraction of the solid phase is tracked with the non-conserved variable, ϕ (where $\phi = 1$ in the solid and $\phi = 0$ in the liquid), and the local concentrations for Ni, Cr, and the salt are tracked with the conserved variables c_{Ni}, c_{Cr}, and c_S, respectively. The following free energy functional is defined in Equation 1:

$$F = \int_V f_{int} + f_{echem}\, dV \tag{1.1}$$

where f_{echem} is the electrochemical free energy, and f_{int} is the interfacial free energy term. The electrochemical free energy is made up of solid- and liquid-phase free energies f^{sol} and f^{liq}, respectively, weighted by their respective phase fraction:

$$f_{echem} = f^{sol} h(\phi) + f^{liq}(1 - h(\phi)) \tag{1.2}$$

where $h(\phi)$ is a weighting-function:

$$h(\phi) = \frac{1}{2} + \frac{2}{\pi}\left[(2\phi - 1)\sqrt{\phi(1-\phi)} + \frac{1}{2}\arcsin(2\phi - 1)\right] \quad (1.3)$$

which is equal to zero in the liquid phase and unity in the solid phase. The free energy of each phase $\alpha = sol, liq$ is given by:

$$f^{\alpha} = \frac{1}{V_m}\sum_i c_i\left(G_i^{0,\alpha} + RT\ln\left(a_i^{\alpha}\right)\right) \quad (1.4)$$

with species: i = Cr (chromium), Ni (nickel), S (salt) phases: α = liq (liquid), sol (solid), where $G_i^{0,\alpha}$ is the standard state free energy for the pure species i in phase α, a_i^{α} is the associated activity, R is the gas constant, T is the temperature, and V_m is the molar volume. The solid phase was taken to be the reference state (i.e. $G_i^{0,sol} = 0$ for all species, i) and so the electrochemical free energy may be written as:

$$f_{echem} = \frac{1}{V_m}\sum_i c_i\left(\Delta G_i^0 + RT\ln\left(\frac{a_i^{liq}}{a_i^{sol}}\right)\right)(1 - h(\phi)) + \frac{1}{V_m}\sum_i c_i\left(RT\ln\left(a_i^{sol}\right)\right) \quad (1.5)$$

where ΔG_i^0 is the Raoultian standard state redox reaction formation energy $\Delta G_i^0 = G_i^{0,liq} - G_i^{0,sol}$ for each species.

The activities associated with mixing Cr, Ni, and salt in the solid and liquid phases are unknown. For simplicity, following [41], simulations in this work assumed ideal mixing among all species in each phase, i.e. $a_i^{\alpha} = c_i^{\alpha}$. This assumption, and its effects on phase field predictions in the current work, are examined in Section 4.2 and Supplemental Note 1. The interfacial free energy (Eq. (2)) contains a gradient energy-penalty for the phase and compositions and a double-obstacle potential for the phase:

$$f_{int} = \frac{4\sigma_{SL}}{\eta}\left[\frac{\eta^2}{\pi^2}(\nabla\phi)^2 + \phi(1-\phi)\right] + \frac{1}{2}\sum_i \kappa(\nabla c_i)^2 \quad (2)$$

In the above, σ_{SL} is the solid-liquid interfacial energy of a pure substance, η is the interface width, and κ is the gradient energy penalty for composition.

The corrosion of the Ni-Cr metal was assumed to be diffusion-limited based on [17], and so a local equilibrium was assumed to be maintained at the interface throughout this process. The phase field model was exercised solely to determine the equilibrium compositions in the solid and liquid phases near the interface, and also any excess concentrations that arose within the diffuse interface to lower the excess free energy of the interface, by evolving the phase and composition fields to minimize the free energy functional in Eq. (1.1). In other words, the model was not used to predict the dynamics of the corrosion process.

The model tacitly assumes electroneutrality through an assumption that oxidants are always available at the interface to accept electrons from the oxidizing species and that cation transport in the liquid is always accommodated by the evolving ion concentration (which was not explicitly tracked in this model). To equilibrate the system and characterize the local-equilibrium interface concentration profiles, the multi-phase field dynamic equations are used to evolve the solid phase:

$$\frac{\partial\phi}{\partial t} = -\frac{\pi^2}{8\eta}M_{SL}\frac{\delta F}{\delta\phi}$$

where M_{SL} is a solid-liquid interface mobility, and $\frac{\delta F}{\delta\phi}$ is the functional derivative of the free energy with respect to the phase variable. The compositions are evolved by the continuity equation:

$$\frac{\partial c_i}{\partial t} = \nabla\cdot M_{ij}\nabla\mu_j$$

where $M_{ij} = \frac{DV_m}{RT}c_i\left(\delta_{ij} - c_j\right)$ is the mobility matrix with diffusion coefficient D, and μ_j is the chemical potential of species j given by the functional derivative $\mu_j = \frac{\delta F}{\delta c_j}$. These kinetic equations were simply used to evolve the phase field variables to equilibrium, and so the choice in M_{SL} and D was unimportant. For simplicity M_{SL} and D were set to unity.

The thermodynamic parameters used in the phase field model are given in Table 2. The temperature was chosen to match the experiment, 600 °C. The redox formation energy for Cr, ΔG_{Cr}^0 was chosen to be slightly negative, while for Ni, ΔG_{Ni}^0 is very large and positive. This was based on the assumption that the salt had a EuF_3 concentration that set its corrosion potential to be above the redox potential for Cr but still well below that for Ni – thus setting a condition where Cr was thermodynamically driven to oxidize and dissolve into the salt while Ni is not [12, 42]. ΔG_S^0 for the salt was chosen to be negative enough to prevent solidification of the salt. The molar volume V_m was set to approximately match the molar volumes of Ni and Cr metals. The solid-liquid interfacial energy is not known for the NiCr-FLiNaK interface, but it can be expected to be of the order $\sigma_{SL} = 1\,\frac{J}{m^2}$ as we have set in Table 2. Realistic variations in this choice do not significantly affect our 1D simulation results but could affect the predictions of solid-liquid interface morphology in 2D and 3D simulations. We set the interface thickness parameter to η= 4 nm, and in practice the large driving forces at the interface reduce the thickness to the realistic ~1 nm. The composition gradient energy-penalty, κ, was chosen following [43] to maintain smooth numerically-stable composition fields. The phase field model was initialized as a solid phase alloy with $c_{Ni} = 0.8$ and $c_{Cr} = 0.2$ in contact with a liquid phase with $c_S = 1.0$, as illustrated in Supplemental Data Fig. S2.

3. Results

3.1. Chemical analysis of the salt

The salt is analyzed by ICP-OES for concentration of corrosion products and corrodants, pre- and post- corrosion experiments (Table 3). When 5 wt.% of EuF_3 oxidizing species is added to the salt mixture to drive a spontaneous reaction with NiCr, Cr is expected to selectively oxidize and dissolve into the salt. Two possible reactions with EuF_3 added in FLiNaK are shown in Eqs. (3) and (4).

$$3EuF_3 + Cr \rightarrow 3EuF_2 + CrF_3 \quad (3)$$

$$2EuF_3 + Cr \rightarrow 2EuF_2 + CrF_2 \quad (4)$$

For a complete reaction of the 0.1139(1) g of EuF_3 added to FLiNaK, the corresponding concentration of Cr in the molten salt is 3827(3) and 5731(5) wppm (μg Cr/ g salt) based on reaction in Eq. (3) and reaction in Eq. (4), respectively. The experimental Cr concentration in the salt is 2010(20) wppm. The Ni concentration in the salt is below the threshold of the measurement (< 0.1 wppm) so we conclude no Ni is corroded from the metal upon exposure to EuF_3 + FLiNaK.

Table 2
Parameters used in the phase field model.

Parameter	Value
Temperature, T	600 °C
Reaction energy for Cr oxidation, ΔG_{Cr}^0	$-10\,\frac{kJ}{mol}$
Reaction energy for Ni oxidation, ΔG_{Ni}^0	$100\,\frac{kJ}{mol}$
Reaction energy for formation of salt, ΔG_S^0	$-120\,\frac{kJ}{mol}$
Molar volume, V_m	$6\times10^{-6}\,\frac{m^3}{mol}$
Solid-liquid interfacial energy, σ_{SL}	$1\,\frac{J}{m^2}$
Interfacial thickness, η	4 nm
Composition-gradient energy-penalty, κ	$2.4\times10^{-9}\,\frac{J}{m}$

Table 3
Concentration of corrodant and corrosion products in FLiNaK salt.

	(wppm *)	As-received FLiNaK	Post-corrosion salt	
			Sample 38salt201	Expected
Corrodant:				
EuF_3 ($Eu^{3+} + e^- \rightarrow Eu^{2+}$)	Eu	< 0.1	33 500 (200)	33 560(30) **
Corrosion products:				
CrF_3	Cr	< 0.1	2 010(20)	< 3 827 (3)***
NiF_2	Ni	< 0.1	< 0.1	< 0.1

* wppm = μg metal cation / g of salt sample.
** based on 0.1139(1) g of EuF_3 added pre-corrosion.
*** based on complete consumption of EuF_3 by the reaction: $3EuF_3 + Cr \rightarrow 3EuF_2 + CrF_3$.

3.2. Electron microscopy of the salt corroded Ni-Cr alloy

The ETD-SEM images (Fig. 2) provide topographical details of corrosion damage to the sample surface (Fig. 2b) and the sample cross-section (Fig. 2c). An annular dark field (ADF)-STEM image (Fig. 2d) displays the cross-section pore extracted from the interior of the sample at a depth of ~50 μm from the surface. The surface contains a significant quantity of corrosion pores (indicated in Fig. 2b) arranged along interconnected trenches that are indicative of grain boundaries. The average distance between the surface-level trenches that are decorated by 0.9 (0.4) μm diameter surface-facing corrosion pores is 37.2(9.9) μm. Observing grain boundaries directly on the surface is challenging due to non-uniform topology and the presence of a surface-facing pore network, which obscures potential grain boundary locations. However, grain size analysis reveals an equiaxed grain morphology within the sample cross-section, with an average grain size of 36.8(15.0) μm. This finding is consistent with the distribution of pores resulting from surface-initiated corrosion (see Supplemental Data Fig. S1c,d). One-dimensional worm-hole shaped pores were reported by [21], associated with grain-boundary attack. Percolation de-alloying mechanism studied in the context of microporous structure formation was reported by [27]. The SEM image of the sample cross-section (Fig. 2c) shows pores up to 50 μm depth (measured perpendicular to the salt-metal interface plane). The pores observed in the cross-section are not arranged on grain boundaries; there is no evidence that the pore network is continuous, though serial cross-sectioning would be needed to further probe the pore continuity. Grain boundary attack would likely lead to continuous worm-holes pores [21]; voids formed during dealloying of the grains can lead to discontinuous pores [17].

SEM-EDS maps from the SEM-level surface analysis (Fig. 3) and cross-section analysis (Fig. 4) show elemental compositions in and around the pores. Along the surface trenches, there are regions of increased F, Na, K, and Cr (salt species), and from cross-section analysis, there is presence of K and F in the pores (Fig. 3h). This is indicative of FLiNaK entering the pores. If the salt penetrates the pores, the rate of pore growth may be determined by the rate of transport of reactants and products to and away from the metal salt interface, and thus by

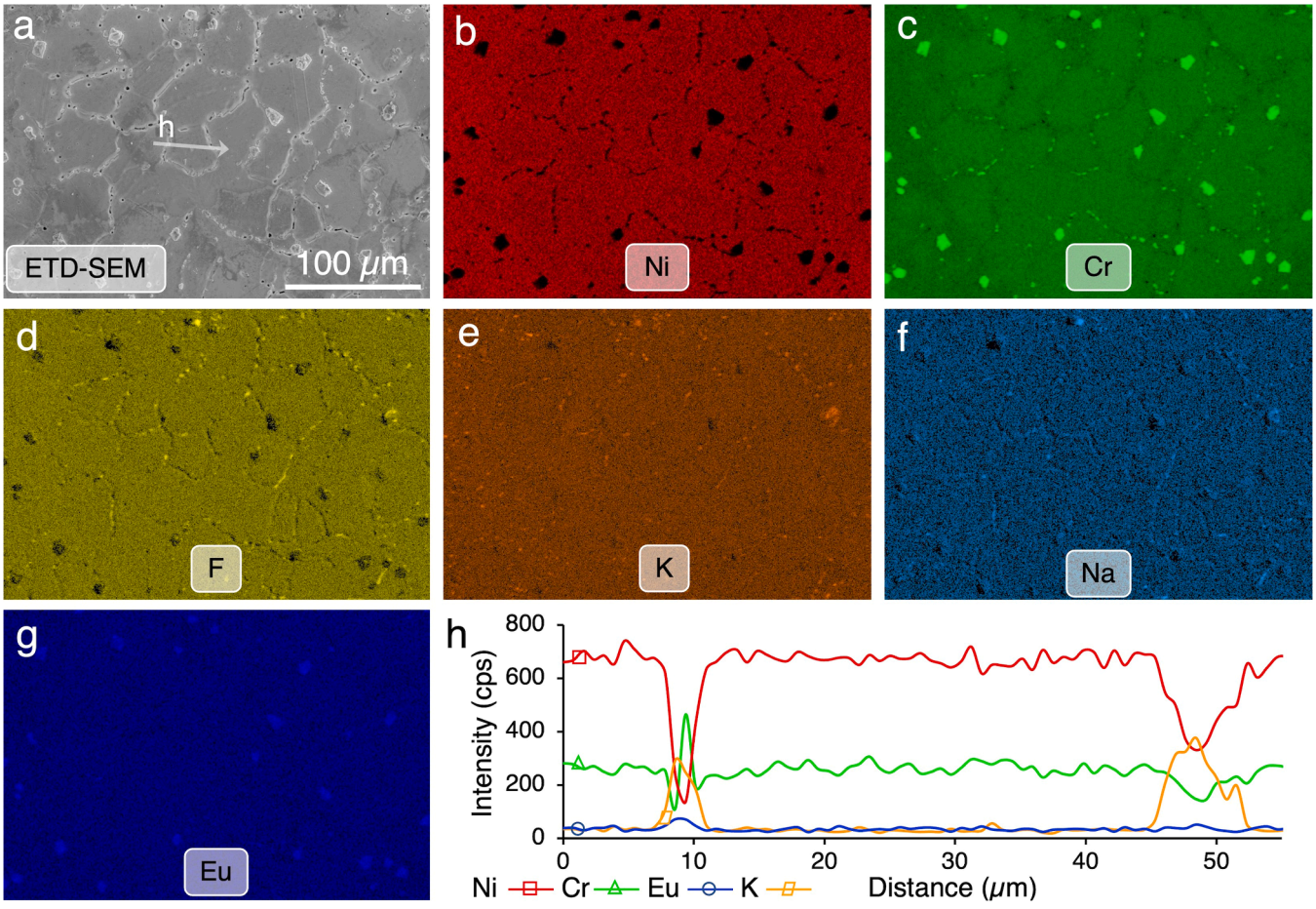

Fig. 3. SEM-EDS of molten salt corroded $Ni_{80}Cr_{20}$ alloy microstructure (a) ETD-SEM image of Ni-Cr sample surface exposed to FLiNaK + EuF_3 salt. EDS X-ray intensity maps for (b) Ni; (c) Cr; (d) F; (e) K; (f) Na; and (g) Eu show microscopic changes in composition around grain boundaries and visible salt-filled pores. (h) EDS line scan taken across two grain boundaries containing corrosion pores displaying X-ray intensity vs. distance indicated by the white dashed line in (a).

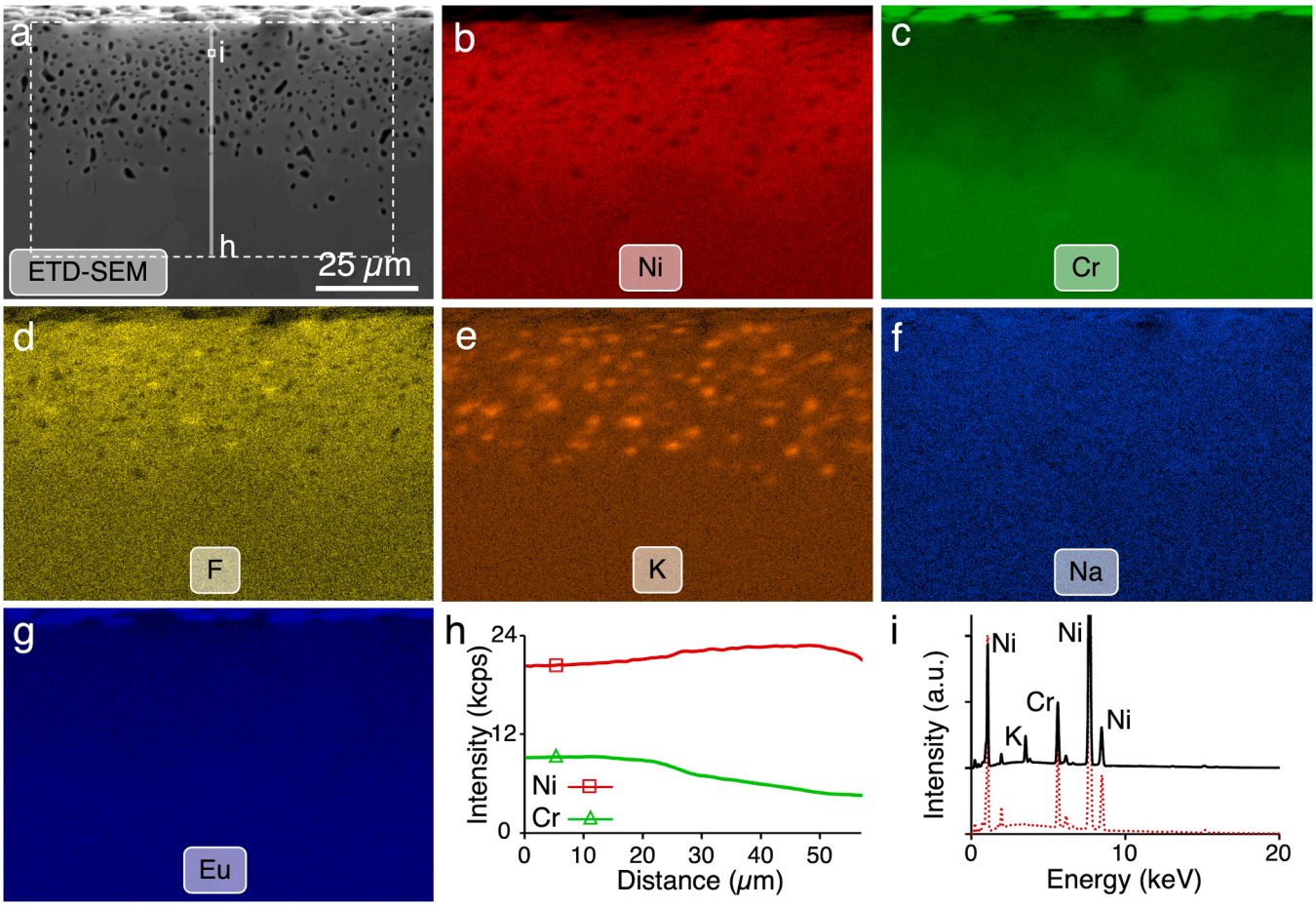

Fig. 4. SEM-EDS of molten salt corroded $Ni_{80}Cr_{20}$ alloy microstructure (a) ETD-SEM image of Ni-Cr sample cross-section with FLiNaK + EuF_3 salt on the top of the image. EDS X-ray intensity maps for (b) Ni; (c) Cr; (d) F; (e) K; (f) Na; and (g) Eu show microscopic changes in composition around salt-filled pores compared to the pristine sample interior at the bottom of the image. (h) EDS line scan displaying X-ray intensity (average intensity extracted from EDS map data within the dashed white box in (a)) vs. distance indicated by the white dashed line in (a). (i) EDS point spectrum (black solid) taken inside a corrosion pore indicated by the white box in (a) with a reference spectrum (red dashed) taken adjacent to the corrosion pore.

diffusivity of Eu3+, Eu2+, and Cr3+ in the molten salt. Micrometer scale Cr-rich features line the grain boundaries (Fig. 3a,c) and are only just visible from the SEM-level resolution. There are 6.8(1.8) μm phases on the sample surface (Figs. 3c and 4c) that are also rich in Cr and in Eu. In addition, nano-scale features speckle the surface of the grains in Fig. 2b, which may have formed in the salt bath during the experiment and deposited on the sample surface, or formed after sample cooling and subsequent exposure to atmosphere. There is no evidence to suggest that they are connected to corrosion pore formation.

Compositional variations between the Ni and Cr are visible in the cross-sectional view (Fig. 4). The Ni composition increases, and the Cr concentration decreases around the interconnected pore region close to the salt-facing sample surface. The composition maps in Fig. 4 indicate a non-uniform pore development that is consistent with the morphology shown in Fig. 2c. There is an enrichment in Ni within the pore structure at the expense of Cr depletion, as observed in the Cr and Ni maps, and in a line scan taken across 50 μm, from the bulk alloy to the salt-facing alloy surface (Fig. 4h). Fig. 4i displays a local EDS area spectrum (black solid) from inside a corrosion pore (white box in Fig. 4a) with an overlay reference spectrum (red dashed) taken adjacent to the corrosion pore. The K-Kα peak in the spectrum from the pore indicates that the pore is filled with salt at the time of analysis. EDS inspection is performed on several other corrosion pores whose cross-sections are positioned farther into the sample and potassium is similarly observed in each of the analyzed pores. The local structure and chemistry at a pore is probed further by FIB lift-out at the measured corrosion depth (Fig. 2c) and subsequent STEM-based analysis Fig. 2d); the lift-out lamella contains Ni-Cr alloy around a pore (~300 nm diameter) containing solidified salt species (FLiNaK + EuF_3).

Fig. 5 presents the ADF-STEM-EDX analysis and nano-beam electron diffraction (NBED) analysis which are used to detail the nanoscale composition and structure, respectively, of phases present around the salt-filled pore. The STEM-EDX overlay map (Fig. 5a) indicates a Ni-rich Ni-Cr alloy matrix (red), Cr-rich regions (green) and Eu-rich salt pore (blue). STEM-EDS line scans (I, II, III) (Fig. 5b) spanning the alloy matrix and the pore indicate the compositional transition from metal alloy (Cr/Ni = 0.1), through the metal-salt interface (up to Cr/Ni = 8) and into the salt-filled pore center. The line scans are arranged to match the transition point between Ni and Cr concentrations as highlighted by the onset of the green regions (Cr-rich regions) from red regions (Ni-rich regions) ~100–200 nm from the edge of the pore. The Cr/Ni ratio is indicated by the right-justified plots (black) above each line scan and calls attention to the shift from Ni-rich to Cr-rich concentrations in the metal; surprisingly, this transition to Cr-rich occurs in the alloy, before transitioning to the salt filled pore. The Cr/Ni ratio plots are truncated where the Ni and Cr concentrations drop below the detection limit of the measurement. The peak in Cr intensity and transition to the salt-filled pore interior, as determined where Ni=0 in the Cr/Ni profile, is illustrated by the point the Cr/Ni plots terminate for each measurement. We use Cr-Kα and Ni-Kα peaks for this analysis, which is not an exact measurement of atomic fraction, but provides a clean signal to show this trend because their energies do not overlap with those of other elements

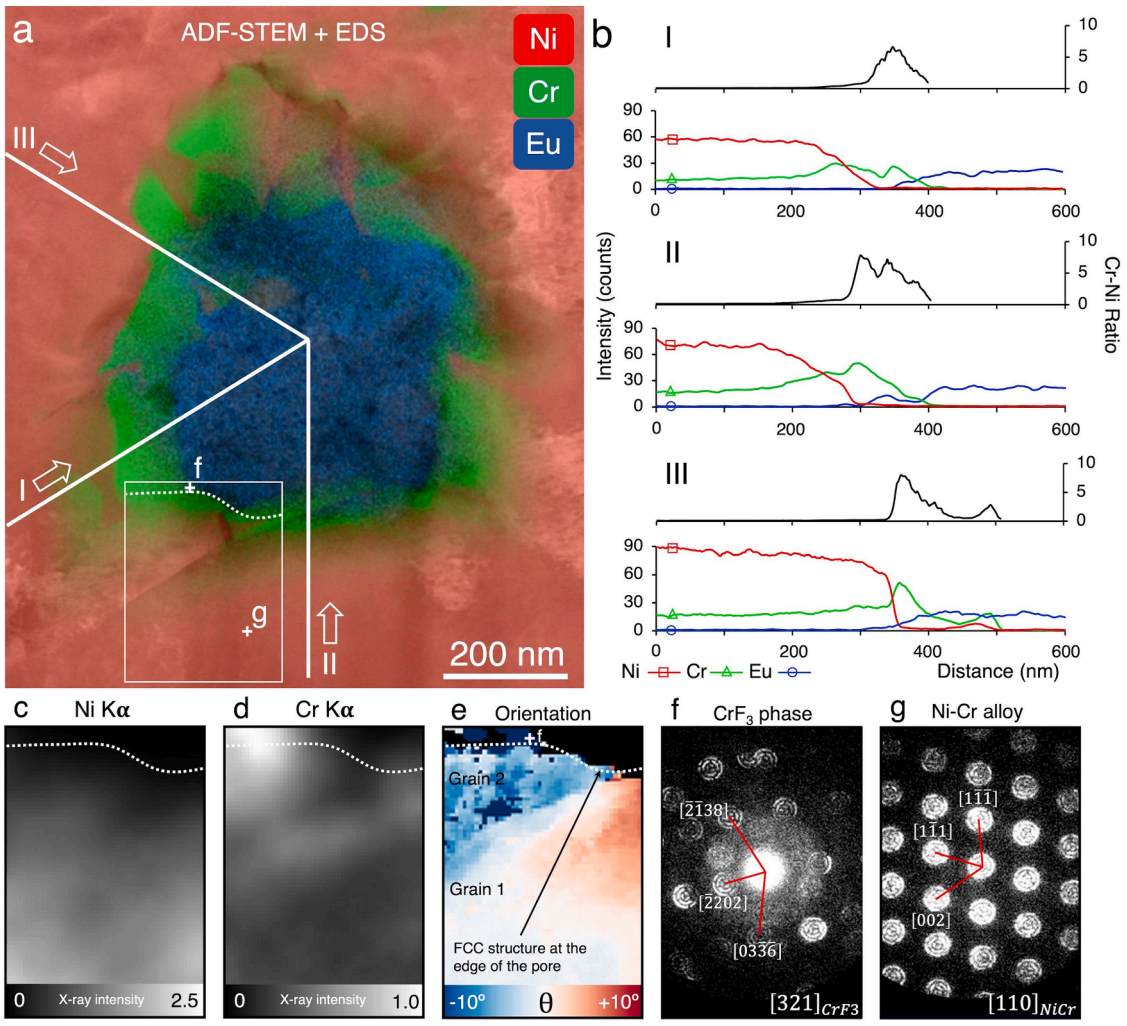

Fig. 5. Composition and structure at the metal-salt interface. (a) STEM-EDX overlay image of Ni (red) Cr (green), and Eu (blue) compositional maps acquired at a salt-filled corrosion pore within the same field of view as Fig. 2d. Cr-rich metal region is identified decorating the salt filled pore (Eu-rich). (b) EDS line scan profiles (I, II, III) taken at the white arrows in (a) show the transition in concentration (atomic fraction) of metal and salt species from the bulk Ni-Cr metal to the salt-filled interior of the pore. Cr – Ni ratio (black) are above each line scan. The plots are truncated where the Ni and Cr concentrations drop below the detection limit of the measurement. (c–e) Simultaneous 4D-STEM / EDX mapping. STEM-EDX X-ray intensity maps show compositional variations of (c) Ni and (d) Cr measured at each pixel location (5 nm x 5 nm). (e) 4D-STEM orientation map taken of the same region coincident with the EDX measurement indicate uniform face centered cubic (FCC) structure within two adjacent grains continuing from the bulk metal to the edge of the pore. (f) Single NBED pattern collected from the top of the 4D-STEM/EDS scan (inset in (a)) is indexed to indicate CrF_3 (trigonal: $R\bar{3}c$) structure. (g) Single NBED pattern collected during the 4D-STEM scan from the pristine metal are indexed to indicate Ni-Cr (cubic: $Fm\bar{3}m$) structure.

present in the system.

Fig. 5(c–e) displays a novel combined measurement taken at two prominent Ni-Cr grains adjacent to the salt-filled pore: STEM-EDX compositional maps and simultaneous structure mapping via 4D-STEM were acquired in the same sample region during the same scan; this combined measurement is used to directly correlate compositional analysis with the crystalline structure, with a spatial resolution of 5 nm. The X-ray intensity maps for Ni (c) and Cr (d) detail a relative compositional variation between the two metallic species from the uncorroded metal alloy (bottom) and showing Cr-enrichment up to the surface of the salt filled pore (top right corner). Within the pore (top right corner), the composition appears dark in both the Ni and Cr maps (absence of both Ni and Cr). Close to the pore edge, there is an increase in Cr signal (bright diffuse band in Fig. 5d) and a diminished Ni signal (dark region in Fig. 5c), as similarly illustrated by the EDS map in Fig. 5a, the EDS line measurements in Fig. 5b. The 4D-STEM orientation map (Fig. 5e) shows two face centered cubic (FCC) structured grains with an 8 – 10 degree difference in orientation that continue up to the edge of the salt filled pore (demarcated, by the curved white dashed line). Notably, this shows that, even with the significant fluctuations in the metal alloy composition (up to Cr/Ni = 8), the structure remains FCC even in the Cr-enriched region (FCC; space group = $Fm\bar{3}m$) up to the salt filled pore. NiO structure (space group = $Fm\bar{3}m$) is nearly identical in structure to FCC Ni-Cr, but with different lattice parameters, thus we exclude the possibility of NiO presence. Further elemental mapping from the 4D-STEM-EDS analysis provided in Supplemental Data Fig. S3 does not show scan positions occupied by Ni that are also occupied by O; therefore, we conclude that NiO phase has not formed in this system. While there is an increase in the presence of local strains approaching the metal-salt interface, there are no clear interfaces with associated misfit dislocations observed with the onset of Cr enrichment, and the structure of Grain 1 shows a continuous grain up to the edge of the corrosion pore.

An additional structure (trigonal; space group = $R\bar{3}c$) is identified in the top of the scan field of view as indicated by the NBED pattern shown in Fig. 5f. The structure closely matches CrF_3 ($a = b = 5$ Å, $c = 13.51$ Å, space group = $R\bar{3}c$) [44] and Cr_2O_3 ($a = b = 4.91$ Å, $c = 13.31$ Å, space group = $R\bar{3}c$). Additional composition and structure information from

the 4D-STEM-EDS analysis is provided in Supplemental Data Fig. S3. Moreover, the phase boundary (dashed white line) illustrates the border of the salt-facing metal and is supported by the transition in structure identified in Supplemental Data Fig. S4. This predominantly uniform FCC structure clearly shows that the regions of Cr enrichment and Ni depletion is nevertheless part of the two Ni-Cr structured grains. Critically, this shows that Cr precipitation and metal plating onto the surface of the pore did not transpire, a finding that would otherwise remain hidden under conventional STEM imaging without correlative chemical and structural analysis. For reference, a single nano-diffraction pattern (Fig. 5g) is taken along the ⟨110⟩ zone axis of the FCC structured Ni-Cr base alloy.

4. Discussion

The corrosion experiment for $Ni_{80}Cr_{20}$ alloy corroded by EuF_3 in molten FLiNaK salt and the characterization of the post-corrosion microstructure displays salt-filled corrosion pores. Observations at the micro- and nano-scale characterize the structure and composition of the salt and the metal alloy at the pore walls.

4.1. Corrosion pore growth and Cr dissolution in FLiNaK

A comparison between elemental analysis by ICP-OES of the salt after corrosion shows removal of 5 mg of Cr metal from the metal alloy sample, leading to a bulk concentration of 2000 wppm Cr in the post-corrosion salt. This indicates that 50 % of the available 0.1 g EuF_3 reduced to EuF_2, oxidizing 5 mg of Cr metal to CrF_3 salt. All nickel is retained in the alloy (< 0.0003 mg of Ni), since no nickel is detected in the post-corrosion salt (< 0.1 ppm).

Figs. 3 and 4 indicate that pore density below the surface is greater than on the surface, and that these sub-surface pores do not necessarily continue to propagate along grain boundaries. Thus, while pore initiation appears as 1D pores and is associated with grain boundaries, consistent with [21], pore growth below the surface is not necessarily governed by high energy sinks or dense point defect networks. Indeed, once the corrosion pores infiltrate deeper into the alloy (further down in Fig. 2c), they tend to proceed away from the grain boundary and into grain interiors. The presence of potassium beneath the surface in Fig. 4 shows that most pores are filled with salt, even approaching their maximum penetration depth.

The growth of pores in de-alloying has been explored for corrosion in aqueous solutions [45] and liquid metals [46]. Liquid metal dealloying (LMD) phase field simulations have been employed to investigate this process within grains [39] and along grain boundaries [43]. In all scenarios, it is generally theorized that the primary mechanisms are the selective dissolution of one element and reorganization of the non-dissolving element(s) through diffusion along the surface of the pore. Importantly, the reorganization of the non-dissolving species is assumed to expose additional dissolving element to the solvent, which reinforces the local corrosion and eventual pore formation. In molten salt corrosion, the dealloying condition is due to the more negative formation energy of CrF_3 compared to NiF_2 in FLiNaK [17,18], and surface diffusion of the Ni, which is assumed to be fast at the metal/salt interface [47]. These processes are assumed to lead to the Cr-dealloyed Ni-rich porous structures seen in the previous experiments.

While this is the case when observing the corroded metal at the 50 μm length-scale, the high-resolution STEM-based observations of the nanoscale structure and composition (Fig. 5) reveal that within 120 nm of the pore surface, the alloy is actually Ni-depleted and Cr-enriched. Further than 200 nm from the interface (Fig. 4) the Ni concentration is enriched relative to the pre-corrosion condition and Cr is depleted. These findings have important implications for the ways in which bulk and interfacial kinetic processes are coupled to govern the corrosion rate and the establishment of complex dealloying morphologies. The possibility of this mechanism leading to positive Cr gradients at the pore surface is illustrated by phase field modeling presented in the next section.

4.2. Phase field modeling of Cr dissolution into molten FLiNaK

The phase field model proposed in the current work reveals a driving force for Cr-enrichment and Ni-depletion at the metal/salt interface. We assume that during the dealloying process, this interface is at a local electrochemical equilibrium between the salt and the metal surface, and we exercise the model to predict this equilibrium condition. This assumption of local equilibrium is based on a previous study of molten salt corrosion, where dealloying was diffusion-limited [17], i.e. that oxidation-dissolution reactions at the interface are fast (compared to bulk-phase transport of products and reactants) and that a ternary composition corresponding to local thermodynamic equilibrium is maintained at the metal and liquid sides of the interface. We consider this to be a reasonable assumption in the present work for the reactions occuring inside the deep corrosion pores that we are considering, where long-range diffusive transport of the corrosion products along the length of the deep, tortuous molten salt channels is required for the corrosion reaction to proceed.

The phase field model prediction of the equilibrium interface between Ni-Cr metal and the molten salt is shown in Fig. 6. Consistent with SEM results in Fig. 4 and the ICP-OES results presented in Table 3, the Ni has a negligible concentration in the salt and is enriched in the corroded region of the alloy. The observed Cr content in the salt is due to the large difference in prescribed formation energies for the metal species in the salt set in Table 2.

Interestingly, in the equilibrium prediction in Fig. 6, the diffuse interface contains an excess Cr concentration that is peaked to approximately 50 at.% in the solid-liquid interface. This can also be explained by the large difference in fluoride formation energies between Ni and Cr in the salt. Specifically, the Ni, having a very large formation energy, has a large energetic penalty associated with being at the interface with the molten salt as Cr oxidizes and dissolves. Since Cr has a more negative formation energy, the excess free energy of the Ni-rich interface can be made lower by introducing an excess Cr concentration. We note that similar predictions have been made by equilibrium models for liquid metal dealloying [48], wherein the dissolving element enriches at the interface between the non-dissolving metal and the liquid that is leaching out the dissolving-metal. In both dealloying scenarios, the models predict that the interface is significantly enriched in the less-noble/dissolving species, having a higher concentration at the interface than in the bulk metal or bulk salt.

In the current work, the excess Cr that arises at the equilibrated interface is not seen to rely on the assumption of ideal mixing between the metal species and the salt. Several phase field simulations that consider non-ideal metal-salt interactions have been run, as detailed in Supplemental Data Note 1. In all simulations, a Cr peak within the interface is always observed, which illustrates that the important thermodynamic characteristic is the large difference in formation energies between the Cr and Ni to dissolve into the molten salt. It should be stated, however, that varying the degree of non-ideal mixing between metal and salt species is likely to affect predictions of corrosion morphology for 2D and 3D simulations. For instance, in other dealloying systems (e.g. LMD) the formation and initial spacing of corrosion channels into the alloy depends on the magnitude of the large, positive mixing enthalpy between the non-dissolving species and the corrosive medium [39,48] and so determining these activities will be crucial to extending the current phase field model to 2D and 3D simulations. Similarly, we note that the Cr-enrichment in this 1D model is not an artifact of the composition-gradient energy-penalty, κ. Rather, this term acts to minimize the effects shown in Fig. 5; when running a simulation with an approximately 50 % lower value for the composition-gradient energy-penalty, the Cr-enrichment was seen to increase to a sharper peak within the interface. However, we note that different choices in this

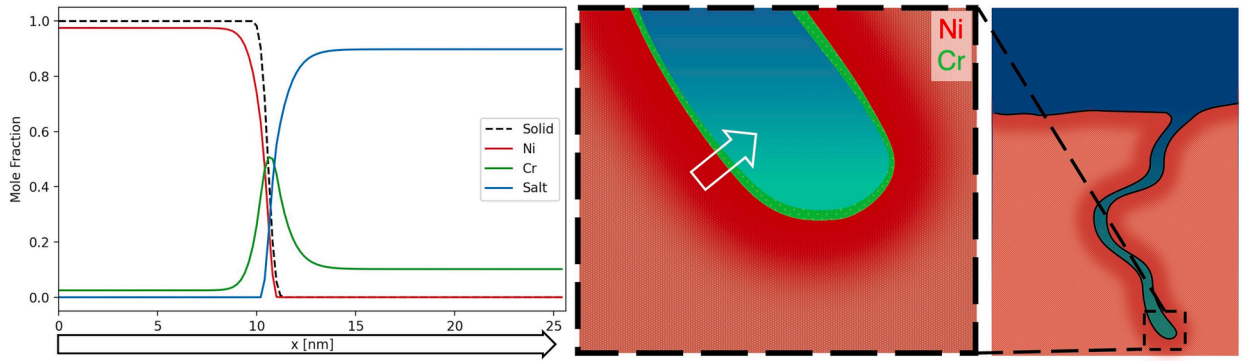

Fig. 6. (left) Phase field model predictions of equilibrium at the solid-liquid interface. The dashed black line corresponds to the volume fraction of the solid phase, and the solid red, green, and blue lines correspond to the composition profiles of Ni, Cr, and the salt species. (right) Schematic illustration modified from Fig. 1 with a magnified view at the bottom of a corrosion pore. Local Cr enrichment (nanoscale) at the surface of the corrosion pore and Ni enrichment (microscale) in metal alloy regions adjacent to the corrosion pore reflect the conclusions drawn from experimental findings and phase field model.

parameter could affect predictions of composition evolution across the interface in a 2D or 3D model, which would also influence the formation and initial spacing of corrosion channels into the alloy [39,48].

The equilibrium Ni and Cr concentration profiles across the solid/liquid interface predicted by the phase field model in Fig. 6 can be compared to the STEM-EDX data presented in Fig. 5. In both instances, there exists a Cr peak at the interface of metal with salt, which decays over some distance into the metal and salt phases. In the phase field model, the excess Cr within the interface decays over a 5 nm distance, while the STEM-EDX line scans in Fig. 5b show that this decay can be much larger (on the order of 50–100 nm). This difference between the experiments and the model would be an interesting topic for future research, but given the difference between the heterogeneous morphology of the actual pore and the 1-dimensional nature of the phase field model, it is not surprising that the spatial components do not match perfectly. Nevertheless, the results from the phase field model show that the difference in each metal's formation potential with the salt can drive chemical rearrangement towards Cr surface-alloying.

4.3. Flux of Ni and Cr species adjacent to metal-salt interface

The composition maps shown at the microscale (Figs. 3 and 4) identify a proposed diffusional pathway in which pores are formed in the corroded region. As Cr is oxidized and transported into the salt, there is a relative decrease in Cr signal from SEM-EDS indicating reduced concentration up to several micrometers from an individual pore. It is noted that in this region of decreased Cr concentration, there is an increase in Ni signal, which suggests that Cr dealloying and formation of voids in the alloy is accompanied by accumulating Ni. However, this does not provide the complete story, as nanoscale composition and structure analysis (Fig. 5) show that within 100 nm of the pore surface, the alloy is primarily Cr-rich metal alloy. The existence of a Cr-rich region is consistent with two possible mechanisms. The first is that the concentration profile from the pore into the bulk material is established by the driving forces associated with selective dissolution of Cr from the metal alloy, conceptually demonstrated by the phase field model in Fig. 6. The second is the thermodynamic response to a temperature change; after corrosion and salt-metal chemical equilibration at high temperature, the temperature change during experiment cooling leads to a change in equilibrium conditions at the metal-salt interface, possibly leading to thickening of the Cr-rich layer.

As previously stated, the selective dealloying of Cr is a consequence of the difference in formation energies between NiF_2 and CrF_3. By evaluating the difference in these energies, the model displayed in Fig. 6 shows that the interface between the salt and the alloy becomes depleted in Ni and higher in Cr as compared to the bulk alloy, due to the comparatively high energetic cost of maintaining a Ni-rich interface with the molten salt. We postulate that in this proposed scenario, the diffusion of Ni back into the alloy could be an important process in the molten salt corrosion of these alloys.

The formation of a Cr-rich phase can also be examined from the perspective of a thermal transient associated with sample cooling. In this case, the equilibrium constant shown in Eq. (5) dictates the activities of both reactants and products from Eq. (3) at steady state.

$$K(T) = \frac{a^3_{EuF_2} \cdot a_{CrF_3}}{a^3_{EuF_3} \cdot a_{Cr_{metal}}} \tag{5}$$

In order to assess the shift of K(T) in response to a temperature transient, the equilibrium constant associated with Eq. (5) was calculated using data from HSC Chemistry v10.2 [49]. As activity coefficients in FLiNaK for europium and chromium fluorides are not well known, thermodynamic data for EuF_3, CrF_3, and EuF_2 is approximated using these species in either the gaseous or aqueous state as analogues for pure compounds and solvated complexes, respectively. A plot of equilibrium constants as a function of temperature is shown in Fig. 7. In both cases, a decreasing equilibrium constant implies a decrease in a_{CrF_3} activity or an increase in $a_{Cr_{metal}}$.

The temperature-dependent equilibrium conditions at the metal-salt interface would drive an increase in $a_{Cr_{metal}}$ and/or a decrease in a_{CrF_3} as temperature decreases. Prior macroscopic observations from corrosion in non-isothermal molten salt flow loops have shown enrichment of Cr at the metal surface during at the lower temperature leg, produced from

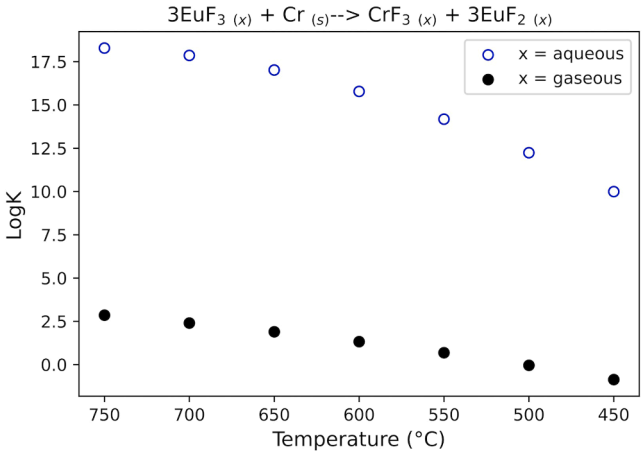

Fig. 7. Decrease of the equilibrium constant associated with Eq. (5) as the salt cools.

the reduction of CrF_3 from the salt when the temperature decreases. This would lead to the deposition of Cr (BCC structure) at the alloy surface. Another mechanism that we postulate here, for the nano-scale gradients that we observe is the diffusion of Cr outwards from the alloy to the surface of the alloy. 4D-STEM structure analysis (hundreds of nanometers from the metal-salt interface) shows no formation of a phase boundary, no local misfit dislocations, and no defined interface. This suggests the FCC Cr-rich metal layer is not a unique precipitated phase, and that the Cr-rich pore-surface layer formed by diffusion of Cr metal from the metal alloy to the pore surface. A third alternative is that if Cr^{3+} is indeed gradually reducing at the salt-metal interface upon temperature decrease and it diffuses back into the metal. The latter would require diffusion of newly reduced Cr metal back into the alloy to compete with nucleation of new Cr grains (BCC crystal structure); no BCC crystal structure is observed.

An extrapolation of Cr diffusion coefficients in $Ni_{80}Cr_{20}$ suggests that the Cr-rich layer (~100 nm thick) revealed in Fig. 5a,b cannot be explained solely by the diffusion of Cr back into the metal during the cooling of the molten salt [50]. Extrapolated from data collected between 950 and 1250 °C, the calculated diffusion coefficient is 1×10^{-20} $\frac{m^2}{s}$ at the maximum observed temperature (600 °C). The diffusion coefficient is applied in $x \approx \sqrt{Dt}$ to estimate the maximum distance of Cr diffusion through the metal during the cooling process. This suggests that Cr can diffuse approximately 5 nm into the metal within a 30-minute period, which corresponds to the observed duration between turning off the furnace and the freezing of the salt at 454 °C. While Cr that has re-entered the metal from the salt may continue to diffuse as the metal continues to cool, with an extrapolated diffusion coefficient at 454 °C (8×10^{-24} $\frac{m^2}{s}$) we conclude that contributions from diffusion at temperatures below the salt melting point are negligible. Thus, while the enrichment of Cr at the metal-salt interface may partly result from diffusion during sample cooling, the thickness of the Cr-rich layer is evidence that diffusion during the temperature decrease is not the primary contributor to its formation. This conclusion is limited by the validity of the extrapolated diffusion coefficient used in the calculation of a maximum diffusion length, either by error introduced through extrapolating sourced data, or by the possible existence of defects introduced through the corrosion process.

Rather than an artifact of experimental cooling, it is posited that the presence of the Cr-rich layer is a consequence of time-dependent diffusion during the corrosion process of $Ni_{80}Cr_{20}$ by EuF_3 in FLiNaK at constant temperature (600 °C). Nanoscale observations of the metal-salt interface within a pore (Fig. 5) support the scenario where interfacial energy is minimized through lattice diffusion from the alloy to the pore surface.

5. Conclusions

In our study, a series of spectroscopy and electron microscopy techniques are implemented to elucidate the role of Cr in the development of deep, tortuous corrosion pores in a FLiNaK molten salt corrosion reaction. The corrosion pores are formed by Cr dissolution and extraction, and the approximate mass loss is consistent with the final amount of Cr in the salt. In contrast, Ni does not deplete from the sample in any considerable amounts, as shown by ICP-OES findings. Cr depletion and Ni enrichment is visible 1–5 μm from corrosion pores. However, there is actually Cr enrichment directly at the metal-salt interface of the pore bottom, as shown by 4D-STEM and EDX measurements and also supported by the phase field model prediction. This finding is attributed to the formation energies associated with the oxidation/dissolution of each alloy species into the molten salt, which is known to be significantly less negative for Ni than Cr. This leads to a high energetic cost associated with maintaining a Ni-rich interface with the molten salt, which can be made less energetic by locally enhancing the Cr-concentration. The STEM-based findings suggest Cr does not precipitate out of salt onto the pore surface. The coupled 4D-STEM / EDX analysis uncovered the Cr lattice diffusion mechanism describing enrichment of Cr at the metal-salt interface.

Together, these methods provide valuable insight to the porosity found during non-uniform corrosion of Ni-Cr salt-facing components in extreme reactor environments by displaying the connections between chemistry and structure at the microscale and nanoscale level. This new information about heterogeneous corrosion pore development allows for more accurate predictions of alloy degradation by revealing the nanoscale interfacial structure and morphology that results from the diffusional-reaction processes expected in reactor extremes. Future work would expand this research to determine if the same Cr enrichment mechanism is applicable in other corrosion regimes of this alloy to consider other variables that are of consideration in reactor environments, such as varying oxidant concentration and the role of nanoscale defects formed by irradiation damage, which play a role in the corrosion rate and morphology. Additionally, the prevalence of this phenomenon could be further understood by applying the 2D and 3D phase field simulations, with the appropriate transport mechanisms informed by atomistic simulations, and proper boundary conditions incorporated. In the development of these models, the present experimental findings of Cr enrichment at the tip of an advancing corrosion pore provide important opportunities for validation.

Data availability

The raw data required to reproduce these findings are available to download from Zenodo (DOI:doi.org/10.5281/zenodo.8000141) and upon reasonable request to the corresponding author.

CRediT authorship contribution statement

Sean H. Mills: Writing – review & editing, Writing – original draft, Methodology, Investigation, Formal analysis, Data curation, Conceptualization. **Ryan D. Hayes:** Writing – review & editing, Methodology, Formal analysis, Data curation. **Nathan Bieberdorf:** Writing – review & editing, Visualization, Methodology, Investigation. **Steven E. Zeltmann:** Software, Data curation. **Alexandra M. Kennedy:** Methodology, Formal analysis, Data curation. **Laurent Capolungo:** Writing – review & editing, Visualization, Methodology. **Mark Asta:** Writing – review & editing, Visualization, Methodology. **Raluca O. Scarlat:** Writing – review & editing, Methodology, Investigation, Conceptualization. **Andrew M. Minor:** Writing – review & editing, Writing – original draft, Supervision, Methodology, Funding acquisition, Conceptualization.

Declaration of competing interests

The authors declare that they have no known competing financial interests or personal relationships that could have appeared to influence the work reported in this paper.

Acknowledgements

Primary support and funding for this work came from FUTURE (Fundamental Understanding of Transport Under Reactor Extremes), an Energy Frontier Research Center funded by the U.S. Department of Energy, Office of Science, Basic Energy Sciences. Work at the Molecular Foundry was supported by the Office of Science, Office of Basic Energy Sciences, of the U.S. Department of Energy under Contract No. DE-AC02–05CH11231. S.E. Zeltmann was supported by STROBE, a National Science Foundation STC funded under grant no. DMR 1548924. This research used resources of the National Energy Research Scientific Computing Center (NERSC), a Department of Energy Office of Science User Facility using NERSC award BES-ERCAP0026478.

Supplementary materials

Supplementary material associated with this article can be found, in the online version, at doi:10.1016/j.actamat.2024.120206.

References

[1] R.C. Newman, K. Sieradzki, Metallic corrosion, Science 263 (1994) 1708–1709.
[2] S. Knight, M. Salagaras, A. Trueman, The study of intergranular corrosion in aircraft aluminium alloys using X-ray tomography, Corros. Sci. 53 (2011) 727–734.
[3] M.P. Enright, D.M. Frangopol, Probabilistic analysis of resistance degradation of reinforced concrete bridge beams under corrosion, Eng. Struct. 20 (1998) 960–971.
[4] F. Cattant, D. Crusset, D. Féron, Corrosion issues in nuclear industry today, Mater. Today 11 (2008) 32–37.
[5] K. Sieradzki, R. Newman, Stress-corrosion cracking, J. Phys. Chem. Solids 48 (1987) 1101–1113.
[6] P.M. Scott, P. Combrade, General corrosion and stress corrosion cracking of Alloy 600 in light water reactor primary coolants, J. Nucl. Mater. 524 (2019) 340–375.
[7] P. Scott, A review of irradiation assisted stress corrosion cracking, J. Nucl. Mater. 211 (1994) 101–122.
[8] S. Lynch, Environmentally assisted cracking: overview of evidence for an adsorption-induced localised-slip process, Acta Metall 36 (1988) 2639–2661.
[9] F. Schmidt, P. Hosemann, R.O. Scarlat, D.K. Schreiber, J.R. Scully, B.P. Uberuaga, Effects of radiation-induced defects on corrosion, Annu. Rev. Mater. Res. 51 (2021) 293–328.
[10] J. Serp, M. Allibert, O. Beneš, S. Delpech, O. Feynberg, V. Ghetta, D. Heuer, D. Holcomb, V. Ignatiev, J.L. Kloosterman, others, The molten salt reactor (MSR) in generation IV: overview and perspectives, Prog. Nucl. Energy 77 (2014) 308–319.
[11] S. Delpech, C. Cabet, C. Slim, G.S. Picard, Molten fluorides for nuclear applications, Mater. Today 13 (2010) 34–41.
[12] S. Guo, N. Shay, Y. Wang, W. Zhou, J. Zhang, Measurement of europium (III)/europium (II) couple in fluoride molten salt for redox control in a molten salt reactor concept, J. Nucl. Mater. 496 (2017) 197–206.
[13] D. LeBlanc, Molten salt reactors: a new beginning for an old idea, Nucl. Eng. Des. 240 (2010) 1644–1656.
[14] C. Andreades, A.T. Cisneros, J.K. Choi, A.Y. Chong, M. Fratoni, S. Hong, L. R. Huddar, K.D. Huff, J. Kendrick, D.L. Krumwiede, others, Design summary of the mark-I pebble-bed, fluoride salt–cooled, high-temperature reactor commercial power plant, Nucl. Technol. 195 (2016) 223–238.
[15] J. Zhang, C.W. Forsberg, M.F. Simpson, S. Guo, S.T. Lam, R.O. Scarlat, F. Carotti, K. J. Chan, P.M. Singh, W. Doniger, others, Redox potential control in molten salt systems for corrosion mitigation, Corros. Sci. 144 (2018) 44–53.
[16] H.L. Chan, E. Romanovskaia, J. Qiu, P. Hosemann, J.R. Scully, Insights on the corrosion thermodynamics of chromium in molten LiF-NaF-KF eutectic salts, Npj Mater. Degrad. 6 (2022) 1–10.
[17] X. Liu, A. Ronne, L.C. Yu, Y. Liu, M. Ge, C.H. Lin, B. Layne, P. Halstenberg, D. S. Maltsev, A.S. Ivanov, S. Antonelli, S. Dai, W.K. Lee, S.M. Mahurin, A.I. Frenkel, J. F. Wishart, X. Xiao, Y. chen K. Chen-Wiegart, Formation of three-dimensional bicontinuous structures via molten salt dealloying studied in real-time by in situ synchrotron X-ray nano-tomography, Nat. Commun. 12 (2021) 1–12, https://doi.org/10.1038/s41467-021-23598-8.
[18] L.-C. Yu, C. Clark, X. Liu, A. Ronne, B. Layne, P. Halstenberg, F. Camino, D. Nykypanchuk, H. Zhong, M. Ge, others, Evolution of micro-pores in Ni–Cr alloys via molten salt dealloying, Sci. Rep. 12 (2022) 20785.
[19] K. Sridharan, T. Allen, Corrosion in molten salts, Molten Salts Chem (2013) 241–267.
[20] D. Olander, Redox condition in molten fluoride salts: definition and control, J. Nucl. Mater. 300 (2002) 270–272.
[21] Y. Yang, W. Zhou, S. Yin, S.Y. Wang, Q. Yu, M.J. Olszta, Y.-Q. Zhang, S. E. Zeltmann, M. Li, M. Jin, others, One dimensional wormhole corrosion in metals, Nat. Commun. 14 (2023) 988.
[22] T. Ghaznavi, S.Y. Persaud, R.C. Newman, The Effect of Temperature on Dealloying Mechanisms in Molten Salt Corrosion, J. Electrochem. Soc. 169 (2022) 111506.
[23] A. Ronne, L. He, D. Dolzhnikov, Y. Xie, M. Ge, P. Halstenberg, Y. Wang, B. T. Manard, X. Xiao, W.-K. Lee, others, Revealing 3D morphological and chemical evolution mechanisms of metals in molten salt by multimodal microscopy, ACS Appl. Mater. Interfaces 12 (2020) 17321–17333.
[24] B. Grégoire, C. Oskay, T. Meißner, M. Galetz, Corrosion mechanisms of ferritic-martensitic P91 steel and Inconel 600 nickel-based alloy in molten chlorides. Part II: naCl-KCl-MgCl2 ternary system, Sol. Energy Mater. Sol. Cells 216 (2020) 110675.
[25] L. Olson, K. Sridharan, M. Anderson, T. Allen, Intergranular corrosion of high temperature alloys in molten fluoride salts, Mater. High Temp 27 (2010) 145–149.
[26] Y.L. Wang, Q. Wang, H.J. Liu, C.L. Zeng, Effect of grain refinement on the corrosion of Ni-Cr alloys in molten (Li, Na, K) F, Corros. Sci. 109 (2016) 43–49.
[27] X. Liu, K. Bawane, X. Zheng, M. Ge, P. Halstenberg, D.S. Maltsev, A.S. Ivanov, S. Dai, X. Xiao, W.-K. Lee, others, Temperature-Dependent Morphological Evolution during Corrosion of the Ni-20Cr Alloy in Molten Salt Revealed by Multiscale Imaging, ACS Appl. Mater. Interfaces 15 (2023) 13772–13782.
[28] S. Guo, J. Zhang, W. Wu, W. Zhou, Corrosion in the molten fluoride and chloride salts and materials development for nuclear applications, Prog. Mater. Sci. 97 (2018) 448–487.
[29] M. Gibilaro, L. Massot, P. Chamelot, A way to limit the corrosion in the Molten Salt Reactor concept: the salt redox potential control, Electrochim. Acta 160 (2015) 209–213.
[30] D. Sulejmanovic, J.M. Kurley, K. Robb, S. Raiman, Validating modern methods for impurity analysis in fluoride salts, J. Nucl. Mater. 553 (2021) 152972.
[31] Oxford Instruments Nanoanalysis, (2023). nano.oxinst.com (accessed April 21, 2023).
[32] J. Schindelin, I. Arganda-Carreras, E. Frise, V. Kaynig, M. Longair, T. Pietzsch, S. Preibisch, C. Rueden, S. Saalfeld, B. Schmid, others, Fiji: an open-source platform for biological-image analysis, Nat. Methods 9 (2012) 676–682.
[33] C.J. Powell, Evaluation of Formulas For Inner-Shell Ionization Cross Sections, US Government Printing Office Washington, 1976.
[34] J. Wood, D. Williams, J. Goldstein, Experimental and theoretical determination of kAFe factors for quantitative X-ray microanalysis in the analytical electron microscope, J. Microsc. 133 (1984) 255–274.
[35] C. Ophus, Four-dimensional scanning transmission electron microscopy (4D-STEM): from scanning nanodiffraction to ptychography and beyond, Microsc. Microanal. 25 (2019) 563–582.
[36] S.E. Zeltmann, A. Müller, K.C. Bustillo, B. Savitzky, L. Hughes, A.M. Minor, C. Ophus, Patterned probes for high precision 4D-STEM bragg measurements, Ultramicroscopy 209 (2020) 112890.
[37] B.H. Savitzky, S.E. Zeltmann, L.A. Hughes, H.G. Brown, S. Zhao, P.M. Pelz, T. C. Pekin, E.S. Barnard, J. Donohue, L.R. DaCosta, others, py4DSTEM: a software package for four-dimensional scanning transmission electron microscopy data analysis, Microsc. Microanal. 27 (2021) 712–743.
[38] F. De La Peña, E. Prestat, V. Tonaas Fauske, P. Burdet, J. Lähnemann, P. Jokubauskas, T. Furnival, M. Nord, T. Ostasevicius, K.E. MacArthur, others, hyperspy/hyperspy: release v1.7.1, (2022). 10.5281/zenodo.6659919.
[39] P.-A. Geslin, I. McCue, B. Gaskey, J. Erlebacher, A. Karma, Topology-generating interfacial pattern formation during liquid metal dealloying, Nat. Commun. 6 (2015) 8887.
[40] I. Steinbach, F. Pezzolla, A generalized field method for multiphase transformations using interface fields, Phys. Nonlinear Phenom. 134 (1999) 385–393.
[41] C.V. Bhave, G. Zheng, K. Sridharan, D. Schwen, M.R. Tonks, An electrochemical mesoscale tool for modeling the corrosion of structural alloys by molten salt, J. Nucl. Mater. 574 (2023) 154147.
[42] D. Ludwig, L. Olson, K. Sridharan, M. Anderson, T. Allen, High temperature electrochemistry of molten fluoride salt for measurement of dissolved chromium, Corros. Eng. Sci. Technol. 46 (2011) 360–364.
[43] N. Bieberdorf, M. Asta, L. Capolungo, Grain boundary effects in high-temperature liquid-metal dealloying: a multi-phase field study, Npj Comput. Mater. 9 (2023) 127.
[44] J.-E. Jørgensen, W. Marshall, R. Smith, The compression mechanism of CrF3, Acta Crystallogr. B 60 (2004) 669–673.
[45] J. Erlebacher, M.J. Aziz, A. Karma, N. Dimitrov, K. Sieradzki, Evolution of nanoporosity in dealloying, Nature 410 (2001) 450–453.
[46] I. McCue, B. Gaskey, P.-A. Geslin, A. Karma, J. Erlebacher, Kinetics and morphological evolution of liquid metal dealloying, Acta Mater 115 (2016) 10–23.
[47] T. Ghaznavi, M.A. Bryk, S.Y. Persaud, R.C. Newman, Alloying effects in high temperature molten salt corrosion, Corros. Sci. 197 (2022) 110003.
[48] L. Lai, P.-A. Geslin, A. Karma, Microstructural pattern formation during liquid metal dealloying: phase-field simulations and theoretical analyses, Phys. Rev. Mater. 6 (2022) 093803.
[49] A. Roine, Outokumpu HSC chemistry for windows, Chem. React. Equilib. Softw. Extensive Ther-Mochemical Database (1994).
[50] R. Evans III, J. DeVan, G. Watson, Self-diffusion of Chromium in Nickel-Base Alloys, Oak Ridge National Laboratory, 1961.